Predicting the response to CTLA-4 blockade by longitudinal noninvasive monitoring of CD8 T cells

Mohammad Rashidian,[1]* Jessica R. Ingram,[1]* Michael Dougan,[1,2]* Anushka Dongre,[1,4] Katherine A. Whang,[1] Camille LeGall,[1] Juan J. Cragnolini,[5] Brian Bierie,[1] Monica Gostissa,[5] James Gorman,[5] Gijsbert M. Grotenbreg,[5] Atul Bhan,[3] Robert A. Weinberg,[1,4,6] and Hidde L. Ploegh[1,6]

[1]Whitehead Institute for Biomedical Research, Cambridge, MA
[2]Division of Gastroenterology and [3]Department of Pathology, Massachusetts General Hospital, Boston, MA
[4]Ludwig Center for Molecular Oncology at MIT, Cambridge, MA
[5]121Bio, LLC, Lexington MA
[6]Department of Biology, Massachusetts Institute of Technology, Cambridge, MA

Immunotherapy using checkpoint-blocking antibodies against targets such as CTLA-4 and PD-1 can cure melanoma and non–small cell lung cancer in a subset of patients. The presence of CD8 T cells in the tumor correlates with improved survival. We show that immuno–positron emission tomography (immuno-PET) can visualize tumors by detecting infiltrating lymphocytes and, through longitudinal observation of individual animals, distinguish responding tumors from those that do not respond to therapy. We used ^{89}Zr-labeled PEGylated single-domain antibody fragments (VHHs) specific for CD8 to track the presence of intratumoral CD8^{+} T cells in the immunotherapy-susceptible B16 melanoma model in response to checkpoint blockade. A ^{89}Zr-labeled PEGylated anti-CD8 VHH detected thymus and secondary lymphoid structures as well as intratumoral CD8 T cells. Animals that responded to CTLA-4 therapy showed a homogeneous distribution of the anti-CD8 PET signal throughout the tumor, whereas more heterogeneous infiltration of CD8 T cells correlated with faster tumor growth and worse responses. To support the validity of these observations, we used two different transplantable breast cancer models, yielding results that conformed with predictions based on the antimelanoma response. It may thus be possible to use immuno-PET and monitor antitumor immune responses as a prognostic tool to predict patient responses to checkpoint therapies.

INTRODUCTION

Immune responses, whether harmful or beneficial, are commonly assessed by taking blood samples and measuring the levels of circulating lymphocytes and their products, such as cytokines and immunoglobulins. In humans, access to tumor tissue, spleen, and lymph nodes requires surgical interventions such as biopsies or sampling at autopsy, invasive methods difficult to apply on a large scale. Mouse models that are often used for preclinical studies related to cancer immunology predominantly rely on euthanasia and examination at necropsy of organs and tissues of interest, which does not provide longitudinal information for therapeutic responses. For these reasons, accurate assessments of immune responses remain a challenge.

The field of immuno-oncology has expanded rapidly with the approval of new antibody therapies that target immune checkpoints and of cell-based therapies that use chimeric antigen receptor–expressing T cells (CAR-T cells; Dougan and Dranoff, 2009; Vesely et al., 2011; Baumeister et al., 2016; Holzinger et al., 2016). For certain cancers such as melanoma and non-small-cell lung cancer, immunotherapy has revolutionized clinical treatment and even produced cures (Dougan and Dranoff, 2009; Vesely et al., 2011; Larkin et al., 2015; Baumeister et al., 2016), but the failure of most patients to achieve long-term remission, even in these treatable types of cancer, remains an important obstacle, particularly given the severity of the side effects often associated with checkpoint blockade (Baumeister et al., 2016; Kourie and Klastersky, 2016). To follow and visualize immune responses longitudinally and predict outcome would thus be highly desirable. It may then be possible to stratify patients into responders and nonresponders during the course of immunotherapy, such that decisions to continue or terminate therapy might be refined in case of an equivocal response. In humans, the presence in biopsy specimens of tumor-infiltrating CD8 T cells, rather than tumor-surrounding CD8 T cells, correlates with a favorable re-

*M. Rashidian, J.R. Ingram, and M. Dougan contributed equally to this paper.

Correspondence to Hidde L. Ploegh: hidde.ploegh@childrens.harvard.edu

M. Gostissa and J. Gorman's present address is Agenus Inc., Lexington, MA.

M. Rashidian and H.L. Ploegh's present address is Boston Children's Hospital/Harvard Medical School, Boston, MA.

Abbreviations used: CAR-T cell, chimeric antigen receptor–expressing T cell; CT, computed tomography; DFO, desferrioxamine; PEG, polyethylene glycol; PET, positron emission tomography; p.i., postinjection; ROI, region of interest; scFv, single-chain variable fragment.

The Rockefeller University Press
J. Exp. Med. 2017 Vol. 214 No. 8 2243–2255
https://doi.org/10.1084/jem.20161950

sponse to checkpoint blockade (Sato et al., 2005; Kawai et al., 2008; Yamada et al., 2010).

Positron emission tomography (PET) using labeled antibodies or antibody fragments (immuno-PET) may achieve some of these goals (Weissleder et al., 2016). Immuno-PET can detect CD8 T cells in living mice, either by using retrovirus-transduced human T cells and detection via the murinized TCRβ constant domain with an ^{89}Zr-labeled F(ab')$_2$ fragment (Mall et al., 2016) or, alternatively, by using isotopically labeled ∼55-kD anti-CD8 diabodies, constructed by fusing two identical single-chain variable fragments (scFvs; Tavaré et al., 2016). Anti–mouse CD8 diabodies can detect CD8 T cells not only in lymphoid organs but also in a transplanted tumor after immunotherapy with 4-1BB or anti–PD-L1 checkpoint-blocking antibodies (Tavaré et al., 2016). However, the key question that remains is whether it is possible to predict the outcome of checkpoint blockade therapy, based not only on the presence of CD8 T cells but also on their numbers, intratumoral distribution and perhaps most importantly dynamic changes in these parameters over time. We demonstrate that immuno-PET can achieve this goal.

To accomplish noninvasive monitoring of the distribution of CD8 T cells, we made use of the smallest antibody-derived format that retains antigen-binding capability, the variable region segment of camelid heavy chain-only antibodies, also referred to as VHHs, nanobodies, or single-domain antibodies (Fig. 1 A; Saerens and Muyldermans, 2012). These fragments are ∼15 kD in size and readily lend themselves to sortase-catalyzed enzymatic modifications for a variety of purposes, including the installation of radioisotopes for PET imaging (Rashidian et al., 2015a,b; Van Elssen et al., 2017).

RESULTS AND DISCUSSION

Generation of an anti-CD8 single-domain antibody fragment and its characterization

Mononuclear cells from a llama immunized with mouse CD8αβ heterodimer stabilized via a C-terminal leucine zipper were used as a source of RNA to construct a VHH phage display library; this yielded several VHH sequences that bound the mouse CD8 marker with nanomolar affinity. We used one of them, VHH-X118, (kD ∼0.9 nM; Fig. S1) for further characterization and as an imaging agent to track the distribution of CD8 T cells.

VHH-X118 was engineered to contain a sortase recognition tag, LPETG, near its C terminus. Sortase, a transpeptidase, recognizes the LPXTG motif and cleaves the bond between the threonine and glycine residues to form a thioester intermediate. A triglycine-functionalized substrate can then replace the enzyme to yield a protein-LPXT-GGG-R product, where R can be any chemical moiety of interest (Fig. 1 B; Guimaraes et al., 2013). VHH-X118 was site-specifically labeled with Alexa Fluor 647 using sortase (Fig. 1 B). LC-MS and SDS-PAGE analysis confirmed labeling (Fig. 1, C and D).

Freshly prepared splenocytes and lymph node cells were stained with Alexa647-labeled VHH-X118 and costained with fluorescent antibodies against the CD45, CD3, CD19, and CD4 markers to identify the relevant lymphocyte subsets. Cytofluorimetry showed that VHH-X118 indeed stained CD8 T cells (Fig. 1 E). Cells did costain with a commercial anti-CD8β antibody. When costained with a commercial anti-CD8α antibody, VHH-X118 effectively competed for binding (Fig. S1), showing that VHH-X118 binds to the CD8α chain.

Improving anti-CD8 VHH for immuno-PET by PEGylation

Using sortase, we installed desferrioxamine (DFO) at the C terminus of VHH-X118 to enable chelation of ^{89}zirconium (^{89}Zr; $t_{1/2}$ = 3.27 d) as a PET tracer (Fig. S2). We performed PET imaging on C57BL/6 mice with ^{89}Zr-VHH-X118 and observed robust and specific accumulation of label in lymphoid organs (Fig. 2 and Video 1). Uptake of ^{89}Zr-VHH-X118 in the kidney was high, a pattern commonly seen for labeled VHHs (Vegt et al., 2010; D'Huyvetter et al., 2014).

Accumulation of VHHs, scFvs, and similar antibody fragments in kidneys and other organs of elimination, such as liver and intestines, produces suboptimal signal-to-noise ratios and complicates the straightforward analysis of tumors growing at or near these anatomical locations (Knowles et al., 2014; Wu, 2014; Rashidian et al., 2015a). Translation of these smaller antibody formats to clinical use may benefit from addressing this particular drawback. We reasoned that the hydrophilic nature of a polyethylene glycol (PEG) substituent might reduce accumulation of ^{89}Zr-labeled VHH in organs of elimination (Li et al., 2010, 2011). We therefore explored sortase-catalyzed PEGylation of ^{89}Zr-labeled VHHs as a means of improving image quality. Site-specific modification of a VHH with PEG in a sortase reaction should leave its antigen-binding site unobstructed, as the PEG modification will be located at a site opposite to the complementarity-determining regions of the VHH (Rashidian et al., 2016). By extending circulatory half-life, PEGylation would further increase the probability of a VHH finding its target in the proper orientation. We therefore designed VHHs modified with PEG moieties that varied in molecular weight from 5 to 20 kD to determine the optimal size of a PEG substituent consistent with an acceptable signal-to-noise ratio. VHHs with modifications in this size range should still be cleared reasonably efficiently by glomerular filtration (cutoff <60 kD).

We synthesized a biorthogonal sortase substrate containing both an azide click handle and the metal chelator DFO (Fig. 2, A and B). The click handle allowed covalent attachment of dibenzylcyclooctyne-substituted PEG moieties of 5, 10, and 20 kD, respectively, all of which showed improved lymph node staining and decreased kidney uptake compared with non-PEGylated VHH-X118 (Fig. 2, C–F; Fig. S2; and Videos 2, 3, 4, and 5). At 24 h postinjection (p.i.), images obtained for the 20-kD PEGylated VHH-X118 showed crisp staining of lymphoid organs, including the mesenteric

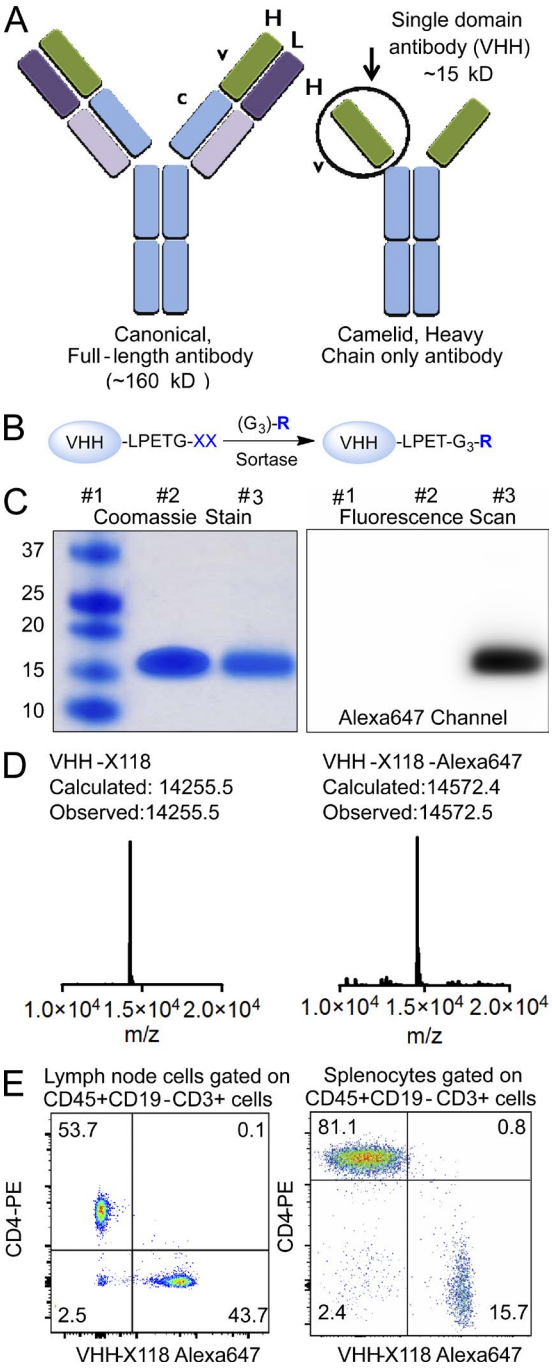

Figure 1. **Characterization of CD8-specific single domain antibody.** (A) Representation of a camelid heavy-chain-only antibody and a conventional IgG. The VHH portion is indicated. (B) Site-specific labeling of VHHs using sortase. (C and D) characterization of X118-VHH and Alexa647-labeled X118-VHH, where SDS-PAGE (C) and LC-MS (D) analysis confirming the identity of the final products (lane 1, marker; lane 2, VHH-X118; lane 3, VHH-X118-Alexa647). (E) FACS analysis of splenocytes and lymph nodes gated on $CD45^+CD19^-CD3^+$ cells confirming that X118-VHH stains $CD8^+$ cells. Results are representative of three to four experiments with similar results.

lymph node, with much reduced accumulation in the kidneys (Fig. 2 F). It was therefore used for all further studies.

Specificity and sensitivity of the anti-CD8 PET signal

To establish specificity of staining with ^{89}Zr-labeled 20-kD PEGylated VHH-X118, we used RAG-KO mice, which lack B and T cells altogether but continue to form $CD8^+$ DCs (Mombaerts et al., 1992). With the exception of a weak signal in the spleen, likely from these $CD8^+$ DCs, there was almost no accumulation of label in lymphoid organs (Fig. 2 G and Video 6), demonstrating specificity of the signal observed in wild-type animals.

We also imaged OT-I-RAGKO TCR transgenic mice, in which all T cells are $CD8^+$ (Hogquist et al., 1994), and we observed a pattern of label accumulation comparable to that seen in wild-type mice, with the exception of a strong signal for an enlarged mesenteric lymph node, a known feature of this particular transgenic model (Fig. S3 and Video 7). To estimate the number of CD8 T cells that could be detected using ^{89}Zr-PEGylated VHH-X118, we excised lymph nodes

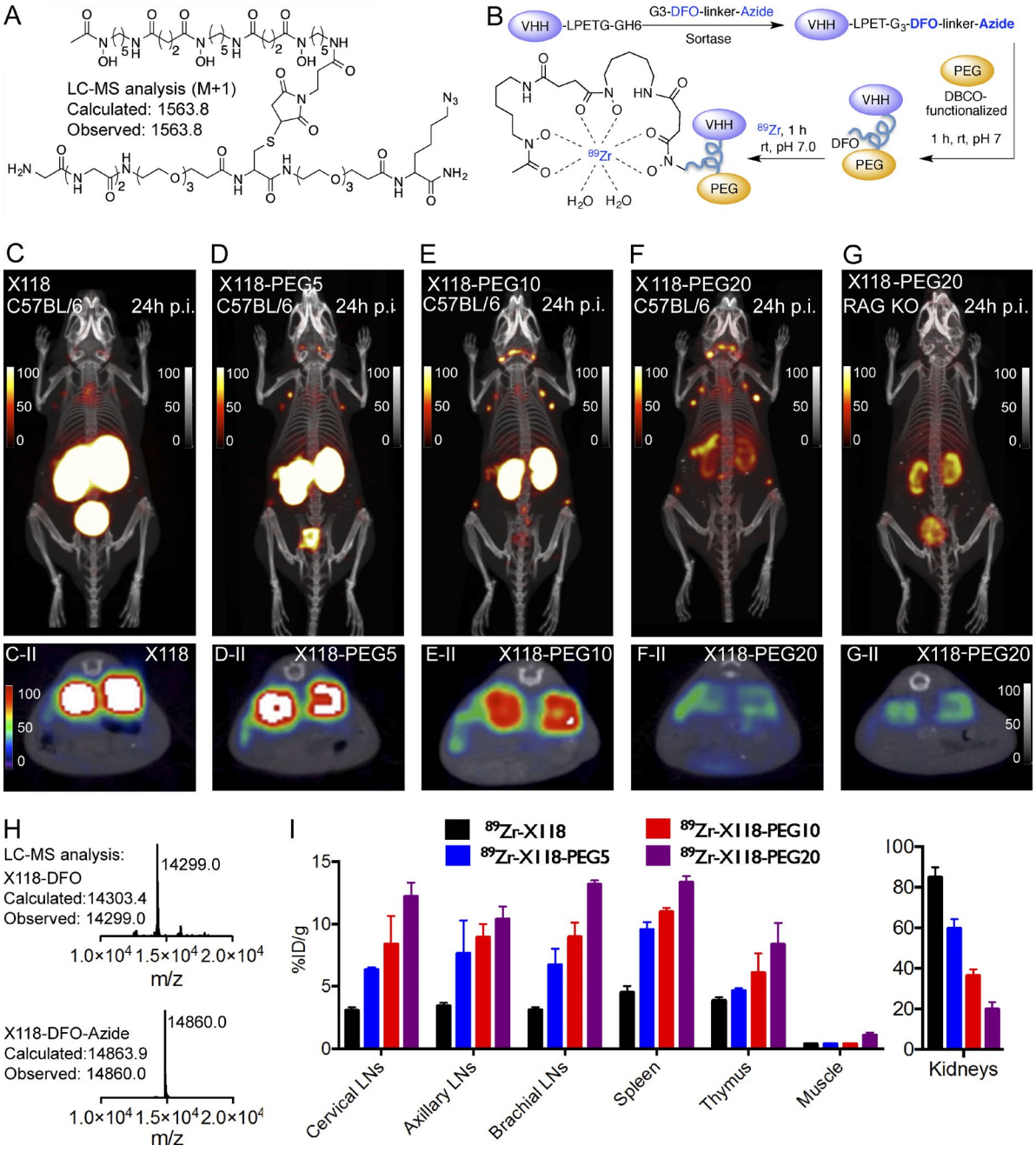

Figure 2. **^{89}Zr-labeled PEGylated anti-CD8 VHH detects CD8 T cells.** (A) Structure of the biorthogonal sortase substrate. The azide functionality allows installation of PEG groups, and the DFO chelator is used to install ^{89}Zr for PET imaging. (B) Schematic representation of preparing PEGylated ^{89}Zr-labeled VHHs for PET imaging. (C–G and C-II–G-II) PET-CT images of anti-CD8 ^{89}Zr-labeled X118-VHH with and without different-size PEG functionalities in wild-type C57BL/6 and RAG-KO mice (n = 3 for each experiment). Images were acquired 24 h p.i. of radiolabeled VHHs. (C-II–G-II, top) Whole-body maximum intensity projections. (C-II–G-II, bottom) Transverse PET-CT images of cross sections through the spleen, showing specific staining and a reduction in accumulation of label in the kidney with increasing PEG size. (H) Characterization of functionalized VHHs. LC-MS analysis confirms formation of X118-DFO and X118-DFO-azide. (I) Biodistribution of anti-CD8 X118-VHH with and without different-size PEGs 24 h p.i. (n = 3 for each cohort). Error bars represent standard deviation.

and spleen and enumerated CD8 T cells per milligram wet weight by cytofluorometry. Lymph nodes contained ∼%16 CD8 T cells, with ∼100,000 CD8 T cells per milligram wet weight. When the amount of radioactivity accumulated per unit weight of muscle was considered to represent the nonspecific background signal and was set at unity, we found >15

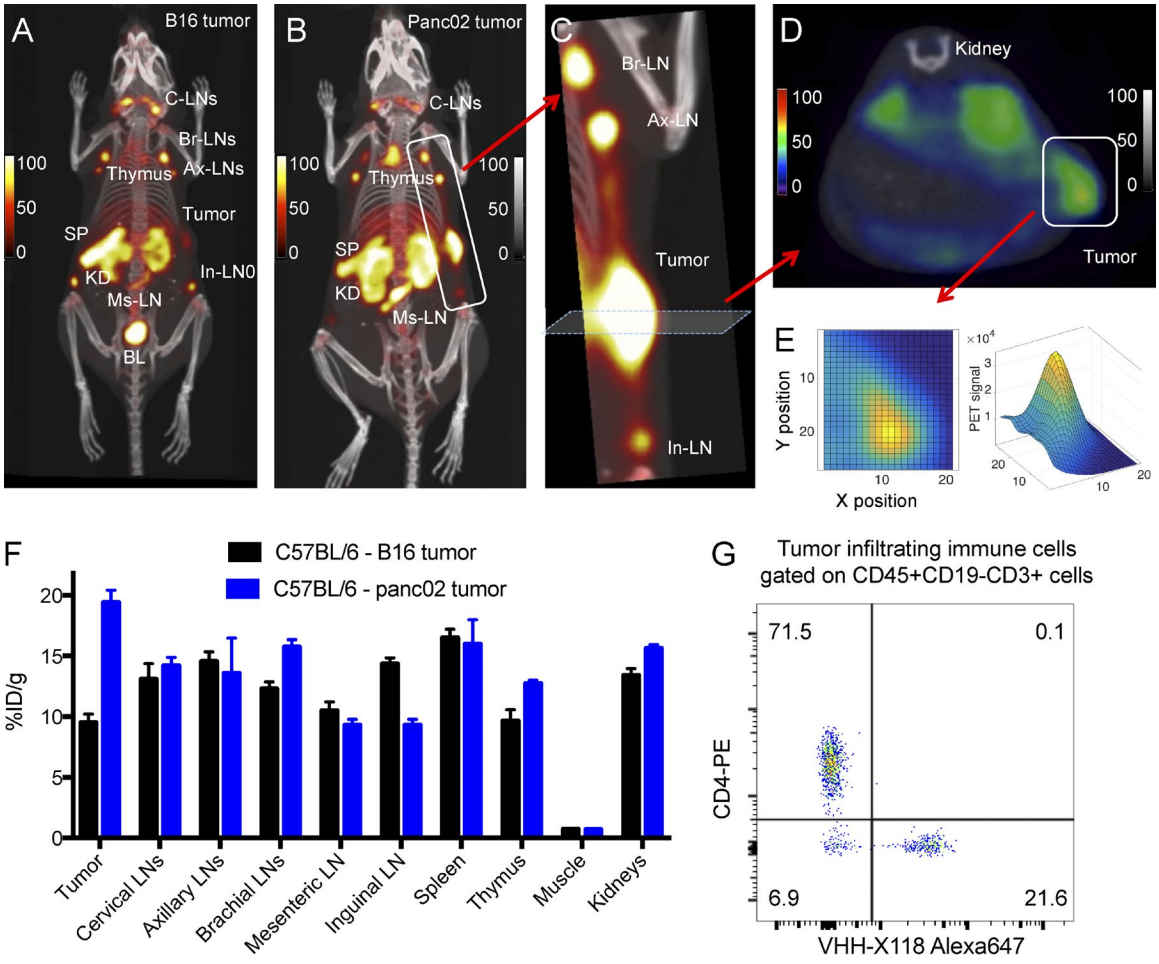

Figure 3. **Anti-CD8 ^{89}Zr-labeled PEG20-X118-VHH detects lymphoid organs and tumor-infiltrating CD8$^+$ lymphocytes.** (A and B) PET-CT images of tumor-bearing mice (A, B16 tumor; B, Panc02 tumor) injected with ^{89}Zr-PEGylated VHH (n = 3 for each experiment). (C) Enlarged view of the tumor and draining lymph nodes. (D) A cross-section of the tumor shows the intratumoral distribution of infiltrated CD8$^+$ T cells. (E) Enlarged view 2D and 3D representation of the cross section in D shows CD8$^+$ T cells deep inside the tumor. (F) Biodistribution of PET signals in different organs and in the tumors. Error bars represent standard deviation. (G) Flow cytometry analysis on the Panc02-infiltrating immune cells confirmed infiltration by CD8$^+$ T cells (n = 3).

times more label accumulated in the brachial lymph node (Fig. 2 I). Hence, assuming as acceptable a minimal ratio of signal-to-background of 3, we could detect ~20,000 CD8 T cells per milligram in a typical lymphoid organ. An increase in PET acquisition time and in injected dose is likely to further improve sensitivity.

Detecting tumors by immuno-PET of infiltrated CD8 T cells

We next used ^{89}Zr-PEGylated VHH-X118 to image tumors and determine its performance in detecting intratumoral CD8 T cells. C57BL/6 mice were implanted with B16 melanoma cells and imaged with ^{89}Zr-PEGylated-VHH-X118. Images acquired 24 h p.i. showed the presence of CD8 T cells in lymphoid organs as well as in and around the tumor (Fig. 3 A and Video 8). We next imaged WT B6 mice bearing Panc02 tumors, a mouse pancreatic cancer cell line. It serves as a suitable model to establish the ability of VHHs to penetrate other tumor types (Rashidian et al., 2015b). Mice bearing heterotopically transplanted Panc02 tumors were imaged using ^{89}Zr-PEGylated VHH-X118. Images acquired 24 and 48 h p.i. showed CD8 T cells in lymphoid organs and infiltrating the tumor (Fig. 3, B and C; and Videos 9 and 10). FACS analysis on tumor-infiltrating lymphocytes in this model confirmed the presence of CD8 T cells (Fig. 3 G). Not only did the PEGylated VHH penetrate the tumor, but cross-sections of the tumor also provided precise positional information (Fig. 3, D and E). We concluded that, with this level of resolution, we should be able to distinguish infiltration into a tumor from a distribution more peripheral to an island of neoplastic cells.

Monitoring the dynamics of CD8 T cells in response to therapy

To track the antitumor CD8 T cell response to checkpoint blockade, we used the B16 mouse melanoma model in conjunction with B16 GVAX (Dranoff et al., 1993; Curran et

al., 2010; Sockolosky et al., 2016). In this model, coadministration of B16 together with irradiated B16 cells transfected with GM-CSF allows the tumors to grow, albeit at a reduced rate when compared with the behavior of control B16 tumors implanted alone in their syngeneic C57BL/6 hosts (Dranoff et al., 1993; Sockolosky et al., 2016). When used as adjuvant therapy, GVAX, a lethally irradiated GM-CSF–secreting whole-cell melanoma vaccine, improves the antitumor response. Treatment of animals having received the B16/GVAX combination with an anti-CTLA4 antibody, administered immediately after tumor implantation, mostly results in a complete response to therapy (Quezada et al., 2006; Curran et al., 2010). Instead, we started treatment 7 d after implantation, a setting in which treatment with anti–CTLA-4 leads to early regression in only a subset of animals (~15%). The remainder of the cohort exhibited a wide spectrum of responses, with variable survival rates (Curran et al., 2010). Even so, every mouse that received anti-CTLA4 showed slower tumor growth compared with the untreated controls. Median survival for the cohort that received no treatment was ~18 d (n = 5), whereas the cohorts with weak partial responses and strong partial responses exhibited median survival times of ~40 d and >50 d, respectively (n = 15).

Having established conditions that would lead to variable responses to CTLA-4 therapy, we tested whether intratumoral distribution and evolution of CD8 T cell numbers over time correlated with a therapeutic response in individual mice. Immuno-PET is uniquely suited to address these questions, as no longitudinal noninvasive assessment of the efficacy of antitumor immunotherapy has been possible until now. We inoculated 20 C57BL/6 mice with B16 and B16 GVAX. A week later, all mice carried palpable tumors of similar size (~3–5 mm in diameter). We randomized and assigned 15 animals to anti-CTLA4 treatment, and five animals served as untreated controls. Each animal was then subjected to PET computed tomography (CT) using radiolabeled 20-kD PEGylated VHH-X118 at four different time points (9, 16, 23, and 30 d after inoculation) to monitor tumor growth or regression and to evaluate CD8 T cell infiltration (Fig. 4 A).

After delineating the outline of the tumor based on CT images, we determined the amount of label per voxel to determine more accurately the distribution of CD8 T cells throughout the tumor (Fig. 4, B, E, and F). As an objective measure of homogeneous versus heterogeneous distribution of CD8 T cells, we created random transects through the quantified PET images for each tumor and plotted the first derivative of the function thus obtained. We examined the plots for the presence of either a single maximum or for several local maxima. For the latter, the first derivative shows more than one zero, whereas the former shows a single zero at the position of maximum signal intensity (Fig. 4, E and F). Quantitation of the PET signals for each tumor shows that the critical parameter relevant for prognosis is the distribution of $CD8^+$ T cells, independent of PET signal strength ($P = 0.035$; Fig. S4). We then asked whether these distributions had value in predicting the responses to anti-CTLA4 treatment. In those tumors in which the CD8 PET signal was homogeneously distributed, with a single cluster of CD8 T cells throughout the tumor, mice continued to respond and tumors failed to increase in size or did so very slowly. In contrast, in tumor-bearing hosts with a more heterogeneous distribution of the CD8 PET signal (with two or more clusters of CD8 T cells), tumors grew faster and mice showed worse survival (Fig. 4, C–F; and Fig. S4).

Using the identified patterns of responses to predict the outcome of therapy

To see whether our observations had more general applicability, we performed similar experiments using mouse mammary tumor cells to explore a possible correlation between CD8 T cell infiltration and response to anti-CTLA4 treatment. We used a carcinoma isolated from the widely used MMTV-PyMT transgenic mouse model (Guy et al., 1992). These tumors are phenotypically heterogeneous with respect to epithelial and mesenchymal sectors. Therefore, to assess the differences in immune cell recruitment associated with the more epithelial- or mesenchymal-like carcinoma cells, we sorted the neoplastic cells based on the expression of an epithelial cell adhesion marker (Epcam) to obtain Epcam-high and Epcam-low cell populations. The different sorted subpopulations of carcinoma cells were then each implanted into syngeneic hosts. Tumors arising from Epcam-high carcinoma cells gave rise to well-differentiated adenocarcinomas, whereas those arising from the Epcam-low carcinoma cells produced poorly differentiated sarcomatoid tumors (unpublished data). Two weeks after implantation of either neoplastic Epcam-high or Epcam-low cells, we performed PET imaging using ^{89}Zr-PEGylated VHH-X118 to assess the distribution of CD8 T cells. Although both types of tumor showed CD8 T cell infiltrates, the Epcam-high, well-differentiated tumors showed a homogenous distribution of CD8 T cells, whereas the poorly differentiated, more mesenchymal Epcam-low tumors showed a more heterogeneous distribution, with clusters of CD8 T cells scattered throughout the tumor (n = 3 for each cohort; Fig. 5, A–D). To confirm the specificity of our PET-CT findings, we imaged a set of animals with Epcam-high and Epcam-low tumors using ^{89}Zr-PEGylated VHH-X118, excised the imaged tumors, and then examined these by immunohistochemistry. As predicted by the ^{89}Zr-PEGylated VHH-X118 PET-CT, Epcam-high tumors showed robust CD8 infiltrates into the tumor core, whereas Epcam-low tumors showed minimal CD8 infiltrates that were clustered around the tumor periphery (n = 5 for each cohort; Fig. 6). These results prompted us to ask whether the observed intratumoral distributions, similar to the B16 model characterized above, might have predictive value for the response to checkpoint blockade.

Accordingly, we inoculated 20 individual wild-type B6 mice with one million Epcam-high or Epcam-low cells and then randomly divided each cohort into two subgroups to

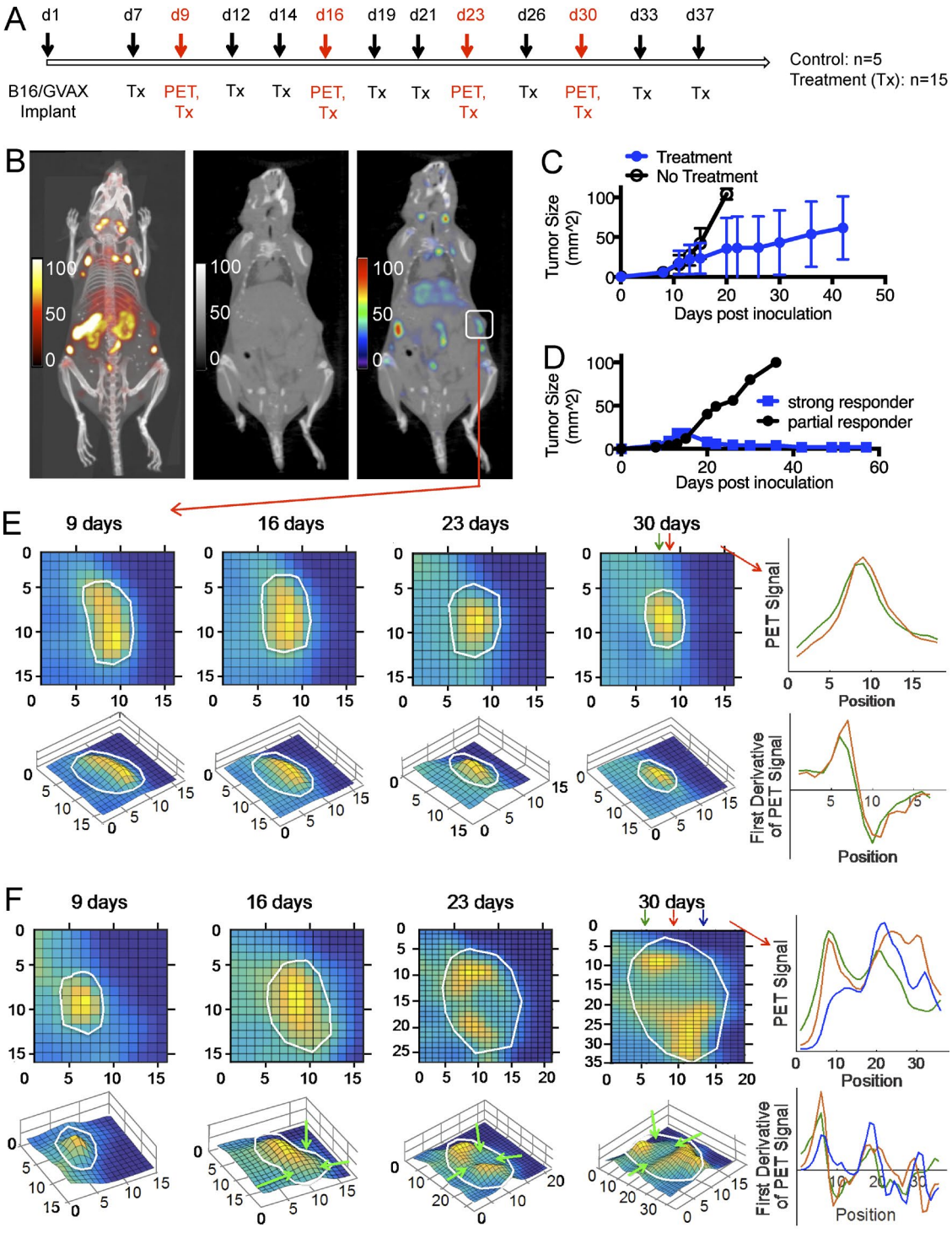

Figure 4. **Dynamics of CD8 T cell response and characterization of response patterns to immunotherapy.** (A) C57BL/6 mice were inoculated with B16 melanoma cells and GVAX simultaneously. Treatment with anti-CTLA4 (clone 9H10) started 1 wk after inoculation to produce a heterogeneous response. Mice received therapy and were subjected to PET imaging according to the schedule shown in scheme A. (B) PET-CT images of a B6 mouse, injected with ^{89}Zr-PEG20-VHH X118, 9 d after inoculation of the tumor. (left) PET-CT maximum intensity projection of the mouse. (middle and right) A coronal cross section CT (middle) or PET-CT (right) image of the mouse. The images are taken through a cross section of the tumor. The box shows the tumor. (C) Mean growth of the tumor in the two cohorts, with or without therapy. Every mouse receiving therapy showed some level of response compared with the untreated cohort, albeit with significant heterogeneity, as evident from the standard deviations. Error bars represent standard deviation. (D) Comparison of the growth of tumors in two mice receiving therapy with a strong or a partial response. (E and F) for animals that received CTLA4 therapy, PET images

receive either anti-CTLA4 (clone 9H10, 200 µg, two times per week for 20 d) or no treatment (n = 5 for each group). Although the well-differentiated, more epithelial tumors with homogenous CD8 T cell distribution responded to anti-CTLA4 treatment, the poorly differentiated, more mesenchymal tumors with heterodisperse CD8 T cell distribution did not, as would be predicted based on the PET results (Fig. 5, E and F). The outcomes of CTLA4 treatment in the two tumor models therefore suggested that immuno-PET might be useful as a predictor of the response. A homogeneous distribution of CD8 T cells could, on its own, serve as an accurate biomarker of future response to anti-checkpoint therapy. These results agree well with immunohistological analysis of human biopsy specimens taken from patients receiving immunotherapy with checkpoint inhibitors, where nonresponding lesions show a peripheral distribution of CD8 T cells and responders show clear signs of CD8 T cells that penetrate the tumor (Sato et al., 2005; Kawai et al., 2008; Yamada et al., 2010).

Invasive procedures such as biopsies cannot provide this type of global information for an entire tumor mass or its metastases and may yield less reliable or even misleading data when correlating immune cell infiltration status with the outcome of immunotherapy. In some instances, a lesion may be heavily infiltrated with immune cells. It may therefore present as an increase in mass in CT scans and be mistaken for an increase in tumor size. Indeed, FDG-PET scans or CT images cannot distinguish between these two, inviting surgery to remove the lesions or even discontinuation of apparently ineffective treatment, when in fact, upon histopathological examination, these masses may turn out to be pure tertiary lymphoid structures containing essentially no neoplastic cells.

Earlier imaging procedures have been limited by several factors. First, these studies only compared treated to untreated mice or, alternatively, examined tumors that expressed or lacked a target antigen of interest (McCracken et al., 2016); this does not recapitulate a typical clinical scenario. Second, tumors previously examined by others were dramatically different in size (McCracken et al., 2016), leaving open the possibility that the observed differences in intratumoral T cell distribution were a consequence rather than the cause of tumor growth and regression, the latter being due, for example, to central tumor necrosis. Finally, previously reported work has not followed T cell distribution longitudinally in individual mice and thus could not provide predictive information.

When assessing the distribution of intratumoral CD8 T cells as determined by PET, there are at least two important parameters to consider. First, tumors that continue to grow in the face of CTLA-4 blockade show heterodisperse accumulation of the intratumoral PET CD8 signal over time. This is consistent with the notion that certain sectors of the tumor might experience a measure of immune privilege, exhaustion, or active immune suppression. Indeed, the absence of a CD8 signal in certain portions of the tumor could result from local contraction of the CD8 pool or from a failure of CD8 T cells to reach that location at all, or it might reflect necrosis. Second, as the nonresponding tumors grow, the focal accumulation of this CD8 signal can change its relative position within the perimeter of the tumor. The local waning of the CD8 signal could reflect contraction of the antigen-experienced pool of CD8 T cells. The emergence of a CD8 signal at a location where previously there was none might result from a clonal burst in situ (e.g., when fresh CD8 T cells migrate into the tumor and then expand). Imaging CD8 T cells by PET thus clearly shows the dynamic nature of these CD8 T cell populations in space and time. Our data cannot address whether the observed changes occur in response to alterations in the tumor or tumor microenvironment or simply reflect intrinsic properties of the T cell response. Sampling the pool of intratumoral CD8 T cells by biopsy and characterizing them for TCR gene usage or specificity will provide a snapshot that is necessarily incomplete with respect to the past and future of the antitumor immune response.

The heterogeneous distribution of CD8 T cells may result from physical barriers, the presence of myeloid-derived suppressor cells releasing repulsive cues (Marigo et al., 2008; Movahedi et al., 2008), the failure of infiltrating CD8 T cells to respond to chemo-attractive signals, hypoxia and hypoxic signaling (McNamee et al., 2013), necrosis or some combination of these factors. We conclude that the ability to image an entire tumor environment noninvasively, making it possible to distinguish between the different distribution patterns of CD8 T cells, may serve as a valuable prognostic indicator of the success of checkpoint blockade therapy. In the future we need to be able to monitor the temporal dynamics of other immune cells, such as CD4 T cells and regulatory T cells, as well as visualize chemokines and cytokines to obtain a more accurate picture of the immune landscape inside and around a tumor. In doing so, we may identify new mechanisms that drive the different

of the tumors are shown. Tumors, as identified by CT, are delineated by the outline. The PET signals in the tumor are rendered as a heatmap. Below each image is the corresponding 3D graph, in which the z axis represents the strength of the PET signal (arbitrary units). On the right side of the PET images are shown PET signal intensities and their first derivatives (below each graph). Two (E) or three (F) different columns, as indicated with arrows, were picked, and graphs were drawn to show the local minima and maxima. The CD8 T cell signal was more homogenously distributed in mice with a strong response to CTLA4 treatment with no local minima throughout the tumor, whereas partial responders showed a more heterogeneous signal distribution with one or more local minima. Where relevant, areas with lower PET signals are indicated by arrows. The images show the dynamics of CD8 T cell throughout the tumors during 4 wk of imaging performed at 9, 16, 23, and 30 d after inoculation of the tumors. The images are representative of multiple experiments with similar results (Fig. S4; n = 15, P = 0.035).

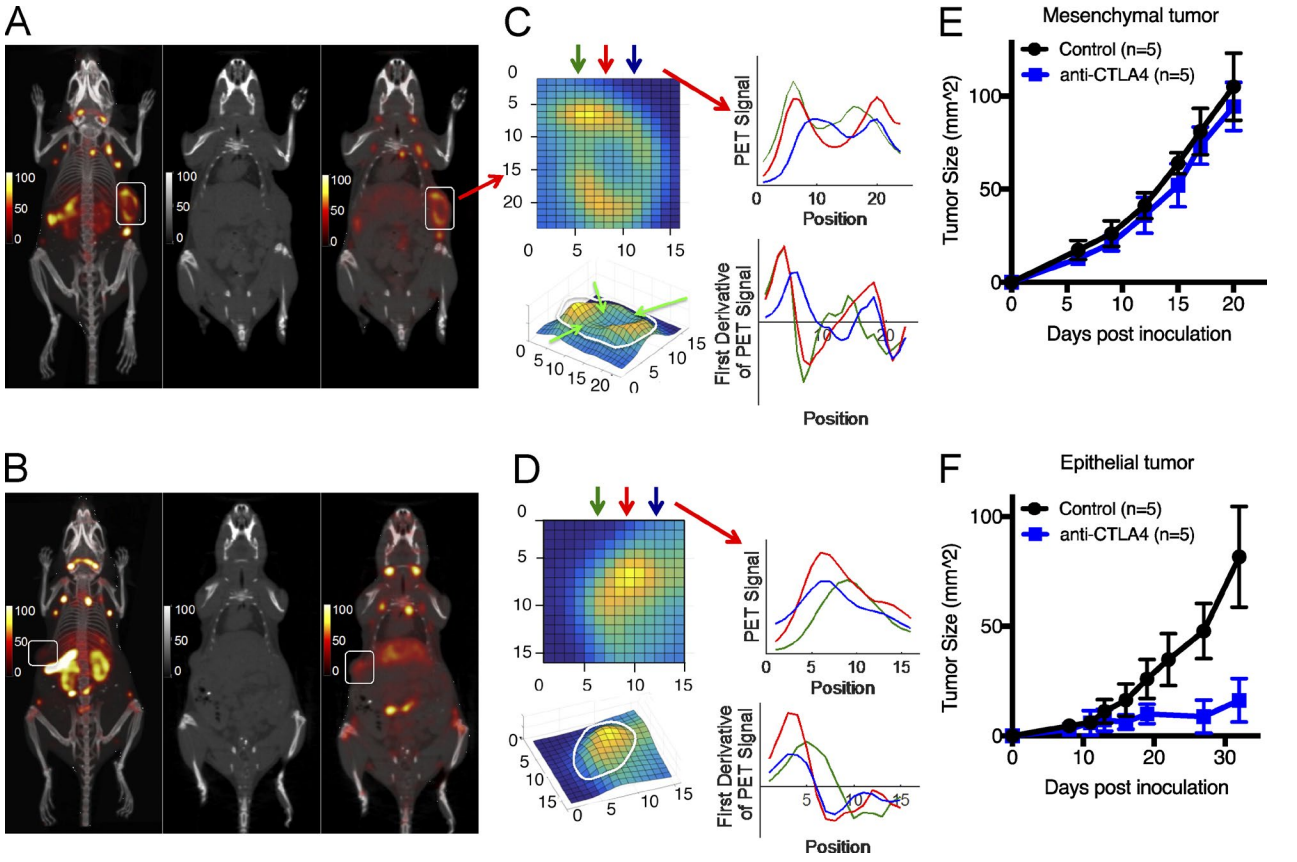

Figure 5. **Predicting the response of immunotherapy in two different breast cancer models.** WT C57BL/6 mice were inoculated with one million breast cancer cells (mesenchymal PB3 cells in A or epithelial PB2 cells in B). 2 wk p.i., mice were imaged by PET/CT using anti-CD8 ^{89}Zr-PEG20-VHH X118. (A) PET-CT images of the mesenchymal tumor-bearing mouse (n = 3); (left) PET/CT maximum intensity projection; (middle and right) coronal CT (middle) and PET-CT (right) images taken through a cross section of the tumor. The box outlines the tumor. (B) PET-CT images of the epithelial PB2 tumor-bearing mice (n = 3). (left) PET-CT maximum intensity projection. (middle and right) Coronal CT (middle) and PET-CT (right) images taken through a cross section of the tumor. (C and D) PET images of the tumors are shown. The PET signals in the tumor are rendered as a heat map. Below each image is the corresponding 3D graph, in which the z axis represents the strength of the PET signal (arbitrary units). The CD8 T cell signal was more homogenously distributed in epithelial tumors, whereas mesenchymal tumors showed a more heterogeneous signal distribution. Where relevant, areas with lower PET signals are indicated by arrows. On the right are graphs that show three randomly chosen transects (arrows) across each of the tumors, plotting the intensity of the PET signal along that transect. The first derivative of this function is shown below each graph to record the presence of local maxima. (E and F) Mean tumor growth with or without receiving therapy. Mice were injected subcutaneously with one million cells (mesenchymal cells in E or epithelial cells in F), followed by 200 µg anti-CTLA4 therapy (clone 9H10) three times per week for 20 d. The epithelial tumors showed a strong response, whereas the mesenchymal tumors did not (n = 5 for each cohort). Error bars represent standard deviation.

types of immune recruitment. Translation of this approach to the clinic may enable earlier identification of treatment response, help distinguish tumor progression from pseudo-progression, and make it possible to iteratively select new therapeutic interventions.

MATERIALS AND METHODS

Animal studies were approved by the MIT Committee on Animal Care (CAC protocol number 1014-110-17).

Generation of the anti-CD8 VHHs

A llama was immunized in a weekly regimen six times with recombinant mouse CD8 (αβ mCD8-leucine zipper; AB Biosciences). VHH libraries were constructed from peripheral blood lymphocytes as described elsewhere (Pardon et al., 2014). Selections were done using a total of three rounds of panning performed on solid-phase immobilized antigen. Randomly selected colonies were analyzed by ELISA for the presence of antigen-specific VHH in their periplasmic extracts. Sequence analysis of ELISA-positive clones yielded 52 candidates. Flow cytometry screening using mCD8 CHO transfectants with αβ 2M peptide (Holst et al., 2006) confirmed eight positives clones.

Analyzing binding affinity of lead VHHs.

Dissociation constants of anti–mouse CD8 were determined by biolayer interferometry (ForteBio Octet RED96 bio-

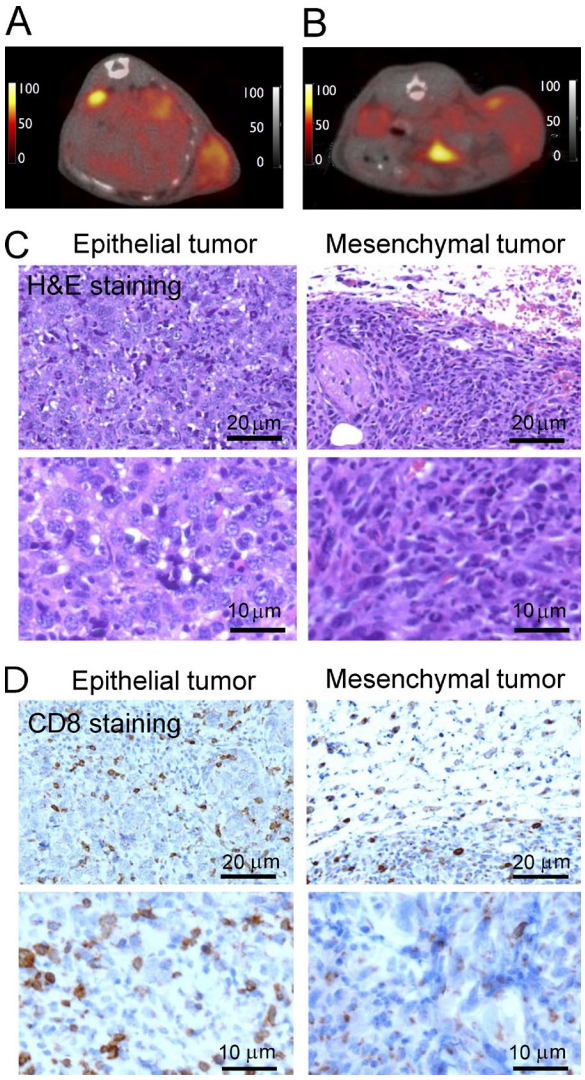

Figure 6. **Correlation of CD8 PET images with immunostaining and histology of tumor sections.** Wild-type C57BL/6 mice were inoculated with one million breast cancer cells (epithelial PB2 cells in A or mesenchymal PB3 cells in B). Mice were imaged 2 wk after inoculation by PET/CT using anti-CD8 ^{89}Zr-PEG20-VHH X118. (A and B) A transverse PET-CT image taken through a cross section of the tumor in mice bearing an epithelial (A) or mesenchymal (B) tumor (n = 5 for each cohort; one representative animal shown). (C) Hematoxylin and eosin (H&E) staining of tumor samples. (D) Immunohistochemistry (CD8$^+$ cells) of paraffin-embedded, formalin-fixed tumor sections shows homogeneous infiltration of CD8$^+$ T cells into PB2 (epithelial tumor). For PB3 (mesenchymal tumor), CD8$^+$ T cells remained mostly peripheral. Top and bottom panels are from the same sections at different magnifications. See supporting information in Fig. S5 for full-size immunohistology and H&E images.

layer interferometer) following the manufacturer's protocol. In brief, recombinant mouse CD8αβ-leucine zipper fusion protein (AB Bioscience) was biotinylated (5:1 biotin/protein) using a Chromalink NHS-Biotin Protein Labeling System (Solulink) and immobilized on a streptavidin sensor. Sensors with immobilized CD8αβ were introduced to a solution containing 25–100 nM anti–mouse CD8 VHH. Binding was allowed to proceed for 90 s, followed by dissociation for 400 s. Unloaded biosensors and a nonspecific VHH were used for background subtraction. Local curve fitting analysis was performed using ForteBio Data Analysis 8.1; dissociation constants (K_D) were calculated using the quotient of the observed association and dissociation rate constants (Fig. S1).

Enzymatic modification of the VHH

Penta mutant sortase A with an improved k_{cat}, was used (Chen et al., 2011). 1-ml reaction mixtures contained 50 mM Tris-HCl, pH 7.5, 10 mM $CaCl_2$, 150 mM NaCl, 750 μM triglycine-containing probe, 200 μM LPETG-containing substrate, and 5 μM sortase (Witte et al., 2012; Theile et al., 2013). After incubation at 4°C with agitation for 30 min, reaction products were analyzed by LC-MS, with yields generally >80%. When the yield was below 80%, the reaction was allowed to proceed for an additional hour, with addition of sortase to 10 μM and triglycine-containing probe to 1 mM. The labeled VHH was purified by size exclusion chromatography in PBS or 50 mM Tris-HCl, pH 7.5. Ni-NTA beads were added to further purify the product followed by centrifugation to remove sortase and any remaining unreacted His-tagged substrate. The labeled protein was stored at −20°C and was stable for up to 6 mo.

Flow cytometry

All antibodies for flow cytometry were obtained from BD (CD3, CD8, CD19, CD4, and CD45). Cells, freshly prepared, were incubated with antibodies at appropriate dilutions for 30 min at 4°C. Analyses were performed on a LSR-Fortessa flow cytometer (BD) and analyzed with CellQuest Pro 6.0 software (BD) and FlowJo version 10 software (Tree Star).

Synthesis of $(Gly)_3$-DFO

The tetrapeptide GGGC was synthesized by standard solid phase peptide synthesis and was dissolved in 20 mM $NaHCO_3$ buffer (pH 8.3). Maleimide-DFO (from Macrocyclics) was dissolved in DMSO. The tetrapeptide GGGC was added and left to stir at room temperature for 30 min until LC-MS analysis indicated near-complete conversion to the product. The solution was filtered and purified by reverse-phase HPLC with a semipreparative column (C_{18} column, Gemini, 5 μm, 10 × 250 mm; Phenomenex) at a flow rate of 5.0 ml/min; solvent A: 0.1% TFA in H_2O, solvent B: 0.1% TFA in CH_3CN. $(G)_3$-DFO eluted at 70–75% solvent B. Fractions containing pure product were collected and lyophilized. LC-MS calculated for $C_{41}H_{71}N_{12}O_{15}S$ $[M+H]^+$ 1003.49, found 1003.70.

Synthesis of $(Gly)_3$-DFO-azide

The peptide GGG-PEG3-Cys-PEG3-Lys(azide) was synthesized by standard solid-phase peptide synthesis and was dissolved in 20 mM $NaHCO_3$ buffer, pH 8.3. Maleimide-DFO was dissolved in DMSO. The peptide was added to the DFO

solution and left to stir at room temperature for 30 min until LC-MS analysis indicated near-complete conversion to the product. The solution was filtered and purified by reverse phase-HPLC with a semi-preparative column (C_{18} column, Gemini, 5 µm, 10 × 250 mm; Phenomenex) at a flow rate of 5.0 ml/min; solvent A: 0.1% TFA in H_2O, solvent B: 0.1% TFA in CH_3CN. $(G)_3$-DFO-azide eluted at 60–65% solvent B. Fractions containing pure product were collected and lyophilized. LC-MS calculated for $C_{65}H_{115}N_{18}O_{24}S$ $[M+H]^+$ 1,563.80, found 1,563.77.

Preparing ^{89}Zr-labeled VHHs

The radiolabeling was performed following an established procedure (Vosjan et al., 2010). In a typical reaction, a solution of 0.5–2.0 mg of chelexed VHH-DFO or PEGylated-VHH-DFO in 200 µl of 0.5 M HEPES buffer, pH 7.5 was prepared. Then a volume of the $^{89}Zr^{4+}$ stock solution (typically supplied in 1.0 M oxalic acid) corresponding to 1.0 to 1.5 mCi was added to a 2 ml plastic screw-cap microcentrifuge tube. The volume of this solution was adjusted to a total of 300 µl using 1.0 M oxalic acid. The pH of the $^{89}Zr^{4+}$ solution was adjusted to 6.8–7.5 using 2.0 M Na_2CO_3. This solution was added to VHH-DFO or PEG-VHH-DFO. The reaction mixture was incubated for 60 min at room temperature on an agitating block at 350 rpm, loaded onto a PD-10 size-exclusion cartridge (GE Healthcare), and eluted with 1× PBS, yielding >80% (~0.8–1.3 mCi) of ^{89}Zr-VHH or PEG-VHH (decay-corrected radiochemical yield).

PET experiments and image analysis

PET-CT procedures have been described in detail elsewhere (Rashidian et al., 2015a). For imaging experiments, mice were anaesthetized using 2.0% isoflurane in O_2 at a flow rate of ~1 liter per minute. Mice were imaged by PET-CT using a G8 PET-CT small-animal scanner (PerkinElmer). Peak sensitivity of the G8 PET-CT accounts for >14% of positron emission, with a mean resolution of 1.4 mm. Each PET acquisition took 10 min, followed by a 1.5-min CT scan. Images were processed using the manufacturer's automatic image reconstruction software. Data were further analyzed and quantified using VivoQuant software. 2D and 3D visualizations were produced using the DICOM viewer (OsiriX Foundation). PET images were viewed side by side with the CT images in DICOM viewer software. Scans were sliced along the coronal plane. A representative image slice that best demonstrated the characteristics of immune cell infiltration for that particular sample was exported as a single DICOM file. Cartesian points that framed the tumor were recorded. The DICOM file was imported into MATLAB and processed with code that read the DICOM file and generated a matrix with PET signal values corresponding to each voxel. The Cartesian points recorded were used to crop the matrix to the tumor section only. 3D shaded surface plots were generated using the MAT LAB function *surf*, where the x and y axes represent points on the image plane and the z axis represents the PET signal value.

For PET quantification, PET images were imported into VivoQuant software. PET signal values were converted into units of percentage of injected dose per gram by using as input the radioactivity at the time of measurement with the preprocessing tool. The CT scan overlaid with PET signal was used as a guide to generate 3D regions of interest (ROIs) to represent a certain organ within the mouse. Depending on the complexity of the ROI, drawing the ROIs was either done free-hand or in automated fashion by setting a threshold value, such that it would capture all connected points with a PET signal above the threshold value. Once all ROIs were generated, a table was exported containing statistical information, such as mean PET signal or variation, for each of ROIs. Clusters of CD8 T cells throughout the tumors were identified by connected voxels, and borders of each cluster were defined as the point at which the derivative of the PET signals became zero (saddle points or local minimums).

To identify local minima and maxima of PET signal within a tumor, we used the same representative image slice used to generate the surface plot mentioned previously. We chose three line segments that intersected the middle of the tumor and used MATLAB to plot the signal intensity along the line segment. With the resulting plot, we approximated the first derivative by calculating the difference between adjacent values of signal intensity versus position on the line segment. A first derivative plot that crossed the x axis only once shows a single local maximum of the PET signal. In contrast, a plot that crossed the x axis two or more times indicates that the PET signal contained multiple local maxima or minima.

Immunohistochemistry

Immunohistochemistry was performed on 5-µm-thick sections deparaffinized to water. Antigen retrieval was done using DIVA solution (Biocare Medical). Endogenous enzyme was blocked for 5 min, and then mouse CD8 (14–0808-80; eBioscience) was incubated at 1:50 in TBS/BSA overnight at 4°C. The following day, HRP rat probe (Rat Probe and Polymer Kit; Biocare Medical) was incubated with the sections for 20 min followed by HRP rat polymer, developed with DAB for 5 min, and then counterstained with hematoxylin.

Mammary tumor models

MMTV-PyMT PB2 and PB3 cells were a gift from the laboratory of H.L. Moses (Vanderbilt-Ingram Cancer Center, Nashville, TN), where they were originally derived by A. Chytil essentially as described previously (Forrester et al., 2005). In brief, MMTV-PyMT mammary tumors from C57BL/6 mice were digested at 37°C for 4 h in serum-free DMEM/F12 + penicillin-streptomycin, amphotericin B, gentamicin, 2 mg/ml collagenase, and 100 U/ml hyaluronidase. Cells were washed with PBS containing 5% adult bovine serum, plated in flasks coated with 50 µg/ml type I collagen, and then maintained in DMEM/F12 medium containing 2% adult bovine serum until they adapted to culture. Cells were adapted to DMEM/F12 medium containing 5% adult bovine

serum with penicillin-streptomycin and nonessential amino acids for the duration of this study.

Online supplemental material

Fig. S1 shows a characterization of VHH-X118. Fig. S2 shows a characterization of PEGylated VHH. Fig. S3 shows PET images of an OT-I RAG-KO mouse. Fig. S4 shows the dynamics of CD8 T cell response and characterization of response patterns to immunotherapy and survival. Fig. S5 shows hematoxylin and eosin staining and immunohistochemistry ($CD8^+$ cells) of tumor samples. Videos 1, 2, 3, 4, and 5 show that 89Zr-VHH-X118, 89Zr-PEG5-VHH-X118, 89Zr-PEG10-VHH-X118, 89Zr-PEG20-VHH-X118, and 89Zr-PEG20-VHH-X118 detect lymphoid organs. Video 6 shows 89Zr-PEG20-VHH-X118 injected into a RAG-KO mouse. Video 7 shows that 89Zr-PEG20-VHH-X118 detects lymphoid organs in OT1-RAGKO mouse. Video 8 shows that 89Zr-PEG5-VHH-X118 detects lymphoid organs and the B16 tumor. Videos 9 and 10 show that 89Zr-PEG5-VHH-X118 detects lymphoid organs and the Panc02 tumor.

ACKNOWLEDGMENTS

We thank Scott Malstrom and Howard Mak of the MIT Koch PET Imaging Facility for technical assistance. We thank Alexander B. Austin of the MIT Koch peptide facility for assistance with peptide synthesis. We thank Vania Kenanova and Bhargavi Ramanathan for helpful discussion regarding PET image analysis. We thank Kyle Fitzgerald and Michael Lofgren for assistance with the biolayer interferometry experiment. We thank Patricia Della Pelle from the Massachusetts General Hospital immunopathology core facility for assistance with immunohistochemistry. We also thank the flow cytometry facility at Whitehead Institute.

Funding was provided by a Cancer Research Institute postdoctoral fellowship (M. Rashidian), a Ludwig Cancer Research postdoctoral fellowship (J.R. Ingram), National Institutes of Health (NIH) training grant 1F32CA210568-01 (M. Dougan), NIH grant R01-AI087879-06 (H.L. Ploegh), NIH Pioneer Award DP1-GM106409-03 (H.L. Ploegh), NIH grant R01-GM100518-04 (H.L. Ploegh), the Lustgarten Foundation (H.L. Ploegh), NIH grant P01 CA080111 (R.A. Weinberg), the Breast Cancer Research Foundation (R.A. Weinberg), the Samuel Waxman Cancer Research Foundation (R.A. Weinberg), and the Ludwig Center for Molecular Oncology (R.A. Weinberg).

M. Gostissa and J. Gorman are employees of Agenus Inc., which owns the X118 single-domain antibody fragment described herein. The remaining authors declare no competing financial interests.

Author contributions: M. Rashidian, J.R. Ingram, and M. Dougan performed or supervised all experiments. A. Dongre and R.A. Weinberg provided specific experimental advice, technical support, and reagents. K.A. Whang, C. LeGall, and B. Bierie provided technical support. J.J. Cragnolini, M. Gostissa, J. Gorman, and G.M. Grotenbreg initially identified and characterized X118. A. Bhan performed the immunohistochemistry. M. Rashidian, J.R. Igram, M. Dougan, and H.L. Ploegh planned all of the experiments, analyzed the data, and wrote the paper with advice from the other authors.

Submitted: 21 November 2016
Revised: 27 March 2017
Accepted: 19 May 2017

REFERENCES

Baumeister, S.H., G.J. Freeman, G. Dranoff, and A.H. Sharpe. 2016. Coinhibitory pathways in immunotherapy for cancer. *Annu. Rev. Immunol.* 34:539–573. http://dx.doi.org/10.1146/annurev-immunol-032414-112049

Chen, I., B.M. Dorr, and D.R. Liu. 2011. A general strategy for the evolution of bond-forming enzymes using yeast display. *Proc. Natl. Acad. Sci. USA.* 108:11399–11404. http://dx.doi.org/10.1073/pnas.1101046108

Curran, M.A., W. Montalvo, H. Yagita, and J.P. Allison. 2010. PD-1 and CTLA-4 combination blockade expands infiltrating T cells and reduces regulatory T and myeloid cells within B16 melanoma tumors. *Proc. Natl. Acad. Sci. USA.* 107:4275–4280. http://dx.doi.org/10.1073/pnas.0915174107

D'Huyvetter, M., C. Xavier, V. Caveliers, T. Lahoutte, S. Muyldermans, and N. Devoogdt. 2014. Radiolabeled nanobodies as theranostic tools in targeted radionuclide therapy of cancer. *Expert Opin. Drug Deliv.* 11:1939–1954. http://dx.doi.org/10.1517/17425247.2014.941803

Dougan, M., and G. Dranoff. 2009. Immune therapy for cancer. *Annu. Rev. Immunol.* 27:83–117. http://dx.doi.org/10.1146/annurev.immunol.021908.132544

Dranoff, G., E. Jaffee, A. Lazenby, P. Golumbek, H. Levitsky, K. Brose, V. Jackson, H. Hamada, D. Pardoll, and R.C. Mulligan. 1993. Vaccination with irradiated tumor cells engineered to secrete murine granulocyte-macrophage colony-stimulating factor stimulates potent, specific, and long-lasting anti-tumor immunity. *Proc. Natl. Acad. Sci. USA.* 90:3539–3543. http://dx.doi.org/10.1073/pnas.90.8.3539

Forrester, E., A. Chytil, B. Bierie, M. Aakre, A.E. Gorska, A.-R. Sharif-Afshar, W.J. Muller, and H.L. Moses. 2005. Effect of conditional knockout of the type II TGF-β receptor gene in mammary epithelia on mammary gland development and polyomavirus middle T antigen induced tumor formation and metastasis. *Cancer Res.* 65:2296–2302. http://dx.doi.org/10.1158/0008-5472.CAN-04-3272

Guimaraes, C.P., M.D. Witte, C.S. Theile, G. Bozkurt, L. Kundrat, A.E.M. Blom, and H.L. Ploegh. 2013. Site-specific C-terminal and internal loop labeling of proteins using sortase-mediated reactions. *Nat. Protoc.* 8:1787–1799. http://dx.doi.org/10.1038/nprot.2013.101

Guy, C.T., R.D. Cardiff, and W.J. Muller. 1992. Induction of mammary tumors by expression of polyomavirus middle T oncogene: A transgenic mouse model for metastatic disease. *Mol. Cell. Biol.* 12:954–961. http://dx.doi.org/10.1128/MCB.12.3.954

Hogquist, K.A., S.C. Jameson, W.R. Heath, J.L. Howard, M.J. Bevan, and F.R. Carbone. 1994. T cell receptor antagonist peptides induce positive selection. *Cell.* 76:17–27. http://dx.doi.org/10.1016/0092-8674(94)90169-4

Holst, J., A.L. Szymczak-Workman, K.M. Vignali, A.R. Burton, C.J. Workman, and D.A.A. Vignali. 2006. Generation of T-cell receptor retrogenic mice. *Nat. Protoc.* 1:406–417. http://dx.doi.org/10.1038/nprot.2006.61

Holzinger, A., M. Barden, and H. Abken. 2016. The growing world of CAR T cell trials: a systematic review. *Cancer Immunol. Immunother.* 65:1433–1450. http://dx.doi.org/10.1007/s00262-016-1895-5

Kawai, O., G. Ishii, K. Kubota, Y. Murata, Y. Naito, T. Mizuno, K. Aokage, N. Saijo, Y. Nishiwaki, A. Gemma, et al. 2008. Predominant infiltration of macrophages and $CD8^+$ T cells in cancer nests is a significant predictor of survival in stage IV nonsmall cell lung cancer. *Cancer.* 113:1387–1395. http://dx.doi.org/10.1002/cncr.23712

Knowles, S.M., K.A. Zettlitz, R. Tavaré, M.M. Rochefort, F.B. Salazar, D.B. Stout, P.J. Yazaki, R.E. Reiter, and A.M. Wu. 2014. Quantitative immunoPET of prostate cancer xenografts with 89Zr- and 124I-labeled anti-PSCA A11 minibody. *J. Nucl. Med.* 55:452–459. http://dx.doi.org/10.2967/jnumed.113.120873

Kourie, H.R., and J. Klastersky. 2016. Immune checkpoint inhibitors side effects and management. *Immunotherapy.* 8:799–807. http://dx.doi.org/10.2217/imt-2016-0029

Larkin, J., V. Chiarion-Sileni, R. Gonzalez, J.J. Grob, C.L. Cowey, C.D. Lao, D. Schadendorf, R. Dummer, M. Smylie, P. Rutkowski, et al. 2015. Combined nivolumab and ipilimumab or monotherapy in untreated

melanoma. *N. Engl. J. Med.* 373:23–34. http://dx.doi.org/10.1056/NEJMoa1504030

Li, L., F. Turatti, D. Crow, J.R. Bading, A.-L. Anderson, E. Poku, P.J. Yazaki, L.E. Williams, D. Tamvakis, P. Sanders, et al. 2010. Monodispersed DOTA-PEG-conjugated anti-TAG-72 diabody has low kidney uptake and high tumor-to-blood ratios resulting in improved 64Cu PET. *J. Nucl. Med.* 51:1139–1146. http://dx.doi.org/10.2967/jnumed.109.074153

Li, L., D. Crow, F. Turatti, J.R. Bading, A.-L. Anderson, E. Poku, P.J. Yazaki, J. Carmichael, D. Leong, D. Wheatcroft, et al. 2011. Site-specific conjugation of monodispersed DOTA-PEGn to a thiolated diabody reveals the effect of increasing peg size on kidney clearance and tumor uptake with improved 64-copper PET imaging. *Bioconjug. Chem.* 22:709–716. http://dx.doi.org/10.1021/bc100464e

Mall, S., N. Yusufi, R. Wagner, R. Klar, H. Bianchi, K. Steiger, M. Straub, S. Audehm, I. Laitinen, M. Aichler, et al. 2016. Immuno-PET imaging of engineered human T cells in tumors. *Cancer Res.* 76:4113–4123. http://dx.doi.org/10.1158/0008-5472.CAN-15-2784

Marigo, I., L. Dolcetti, P. Serafini, P. Zanovello, and V. Bronte. 2008. Tumor-induced tolerance and immune suppression by myeloid derived suppressor cells. *Immunol. Rev.* 222:162–179. http://dx.doi.org/10.1111/j.1600-065X.2008.00602.x

McCracken, M.N., R. Tavaré, O.N. Witte, and A.M. Wu. 2016. Advances in PET detection of the antitumor T cell response. *Adv. Immunol.* 131:187–231. http://dx.doi.org/10.1016/bs.ai.2016.02.004

McNamee, E.N., D. Korns Johnson, D. Homann, and E.T. Clambey. 2013. Hypoxia and hypoxia-inducible factors as regulators of T cell development, differentiation, and function. *Immunol. Res.* 55:58–70. http://dx.doi.org/10.1007/s12026-012-8349-8

Mombaerts, P., J. Iacomini, R.S. Johnson, K. Herrup, S. Tonegawa, and V.E. Papaioannou. 1992. RAG-1-deficient mice have no mature B and T lymphocytes. *Cell.* 68:869–877. http://dx.doi.org/10.1016/0092-8674(92)90030-G

Movahedi, K., M. Guilliams, J. Van den Bossche, R. Van den Bergh, C. Gysemans, A. Beschin, P. De Baetselier, and J.A. Van Ginderachter. 2008. Identification of discrete tumor-induced myeloid-derived suppressor cell subpopulations with distinct T cell-suppressive activity. *Blood.* 111:4233–4244. http://dx.doi.org/10.1182/blood-2007-07-099226

Pardon, E., T. Laeremans, S. Triest, S.G.F. Rasmussen, A. Wohlkönig, A. Ruf, S. Muyldermans, W.G.J. Hol, B.K. Kobilka, and J. Steyaert. 2014. A general protocol for the generation of nanobodies for structural biology. *Nat. Protoc.* 9:674–693. http://dx.doi.org/10.1038/nprot.2014.039

Quezada, S.A., K.S. Peggs, M.A. Curran, and J.P. Allison. 2006. CTLA4 blockade and GM-CSF combination immunotherapy alters the intratumor balance of effector and regulatory T cells. *J. Clin. Invest.* 116:1935–1945. http://dx.doi.org/10.1172/JCI27745

Rashidian, M., E.J. Keliher, A.M. Bilate, J.N. Duarte, G.R. Wojtkiewicz, J.T. Jacobsen, J. Cragnolini, L.K. Swee, G.D. Victora, R. Weissleder, and H.L. Ploegh. 2015a. Noninvasive imaging of immune responses. *Proc. Natl. Acad. Sci. USA.* 112:6146–6151. http://dx.doi.org/10.1073/pnas.1502609112

Rashidian, M., E.J. Keliher, M. Dougan, P.K. Juras, M. Cavallari, G.R. Wojtkiewicz, J.T. Jacobsen, J.G. Edens, J.M.J. Tas, G. Victora, et al. 2015b. Use of ^{18}F-2-fluorodeoxyglucose (FDG) to label antibody fragments for immuno-PET of pancreatic cancer. *ACS Central Science.* 1:142–147. http://dx.doi.org/10.1021/acscentsci.5b00121

Rashidian, M., L. Wang, J.G. Edens, J.T. Jacobsen, I. Hossain, Q. Wang, G.D. Victora, N. Vasdev, H. Ploegh, and S.H. Liang. 2016. Enzyme-mediated modification of single-domain antibodies for imaging modalities with different characteristics. *Angew. Chem. Int. Ed. Engl.* 55:528–533. http://dx.doi.org/10.1002/anie.201507596

Saerens, D., and S. Muyldermans, editors. 2012. Single Domain Antibodies. Humana Press, Totowa, NJ. http://dx.doi.org/10.1007/978-1-61779-968-6

Sato, E., S.H. Olson, J. Ahn, B. Bundy, H. Nishikawa, F. Qian, A.A. Jungbluth, D. Frosina, S. Gnjatic, C. Ambrosone, et al. 2005. Intraepithelial CD8+ tumor-infiltrating lymphocytes and a high CD8+/regulatory T cell ratio are associated with favorable prognosis in ovarian cancer. *Proc. Natl. Acad. Sci. USA.* 102:18538–18543. http://dx.doi.org/10.1073/pnas.0509182102

Sockolosky, J.T., M. Dougan, J.R. Ingram, C.C.M. Ho, M.J. Kauke, S.C. Almo, H.L. Ploegh, and K.C. Garcia. 2016. Durable antitumor responses to CD47 blockade require adaptive immune stimulation. *Proc. Natl. Acad. Sci. USA.* 113:E2646–E2654. http://dx.doi.org/10.1073/pnas.1604268113

Tavaré, R., H. Escuin-Ordinas, S. Mok, M.N. McCracken, K.A. Zettlitz, F.B. Salazar, O.N. Witte, A. Ribas, and A.M. Wu. 2016. An effective immuno-PET imaging method to monitor CD8-dependent responses to immunotherapy. *Cancer Res.* 76:73–82. http://dx.doi.org/10.1158/0008-5472.CAN-15-1707

Theile, C.S., M.D. Witte, A.E.M. Blom, L. Kundrat, H.L. Ploegh, and C.P. Guimaraes. 2013. Site-specific N-terminal labeling of proteins using sortase-mediated reactions. *Nat. Protoc.* 8:1800–1807. http://dx.doi.org/10.1038/nprot.2013.102

Van Elssen, C.H.M.J., M. Rashidian, V. Vrbanac, K.W. Wucherpfennig, Z.E. Habre, J. Sticht, C. Freund, J.T. Jacobsen, J. Cragnolini, J. Ingram, et al. 2017. Noninvasive imaging of human immune responses in a human xenograft model of graft-versus-host disease. *J. Nucl. Med.* 58:1003–1008. http://dx.doi.org/10.2967/jnumed.116.186007

Vegt, E., M. de Jong, J.F.M. Wetzels, R. Masereeuw, M. Melis, W.J.G. Oyen, M. Gotthardt, and O.C. Boerman. 2010. Renal toxicity of radiolabeled peptides and antibody fragments: Mechanisms, impact on radionuclide therapy, and strategies for prevention. *J. Nucl. Med.* 51:1049–1058. http://dx.doi.org/10.2967/jnumed.110.075101

Vesely, M.D., M.H. Kershaw, R.D. Schreiber, and M.J. Smyth. 2011. Natural innate and adaptive immunity to cancer. *Annu. Rev. Immunol.* 29:235–271. http://dx.doi.org/10.1146/annurev-immunol-031210-101324

Vosjan, M.J.W.D., L.R. Perk, G.W.M. Visser, M. Budde, P. Jurek, G.E. Kiefer, and G.A.M.S. van Dongen. 2010. Conjugation and radiolabeling of monoclonal antibodies with zirconium-89 for PET imaging using the bifunctional chelate p-isothiocyanatobenzyl-desferrioxamine. *Nat. Protoc.* 5:739–743. http://dx.doi.org/10.1038/nprot.2010.13

Weissleder, R., M.C. Schwaiger, S.S. Gambhir, and H. Hricak. 2016. Imaging approaches to optimize molecular therapies. *Sci. Transl. Med.* 8:355ps16. http://dx.doi.org/10.1126/scitranslmed.aaf3936

Witte, M.D., J.J. Cragnolini, S.K. Dougan, N.C. Yoder, M.W. Popp, and H.L. Ploegh. 2012. Preparation of unnatural N-to-N and C-to-C protein fusions. *Proc. Natl. Acad. Sci. USA.* 109:11993–11998. http://dx.doi.org/10.1073/pnas.1205427109

Wu, A.M. 2014. Engineered antibodies for molecular imaging of cancer. *Methods.* 65:139–147. http://dx.doi.org/10.1016/j.ymeth.2013.09.015

Yamada, N., S. Oizumi, E. Kikuchi, N. Shinagawa, J. Konishi-Sakakibara, A. Ishimine, K. Aoe, K. Gemba, T. Kishimoto, T. Torigoe, and M. Nishimura. 2010. CD8+ tumor-infiltrating lymphocytes predict favorable prognosis in malignant pleural mesothelioma after resection. *Cancer Immunol. Immunother.* 59:1543–1549. http://dx.doi.org/10.1007/s00262-010-0881-6